materials

MDPI

Article

Low-Temperature Synthesis of Cu-Doped Anatase TiO_2 Nanostructures via Liquid Phase Deposition Method for Enhanced Photocatalysis

Mitsuhiro Honda [1,*], Tsuyoshi Ochiai [2], Popy Listiani [1], Yuma Yamaguchi [1] and Yo Ichikawa [1]

[1] Graduate School of Engineering, Nagoya Institute of Technology, Nagoya 466-8555, Japan
[2] Materials Analysis Group, Kawasaki Technical Support Department, Kanagawa Institute of Industrial Science and TEChnology (KISTEC), Kawasaki 213-0012, Japan
* Correspondence: honda.mitsuhiro@nitech.ac.jp

Abstract: Titanium dioxide (TiO_2) photocatalysis can harness the energy from sunlight, providing a solution to many green- and energy-related problems. In this study, we aimed to produce Cu doped TiO_2 (Cu-TiO_2) structures at a low temperature (~70 °C) under atmospheric pressure based on liquid phase deposition. The products prepared with Cu nitrate exhibited anatase-phase TiO_2 with the presence of Cu, and the particles showed a waxberry-like structure. Changing the Cu nitrate concentration allowed control of the atomic concentration; we confirmed ~1.3 atm.% of Cu ions in the product when we applied 10 mM in the precursor solution. By doping Cu, the light absorption edge shifted to 440 nm (~2.9 eV), and we proved the photocatalytic reaction through action spectral measurement. We observed the decomposition of acetaldehyde into CO_2 on Cu-TiO_2 photocatalysts, which produced optimized improvements in photocatalytic activity at Cu dopant levels between 0.2 and 0.4 atm.%. This study demonstrates that the liquid phase deposition technique can be used for doping metallic ions into TiO_2, which shows promise for preparing novel and unique nanomaterials as visible light photocatalysts.

Keywords: photocatalysis; liquid phase deposition; copper doping; low-temperature synthesis

check for updates

Citation: Honda, M.; Ochiai, T.; Listiani, P.; Yamaguchi, Y.; Ichikawa, Y. Low-Temperature Synthesis of Cu-Doped Anatase TiO_2 Nanostructures via Liquid Phase Deposition Method for Enhanced Photocatalysis. *Materials* **2023**, *16*, 639. https://doi.org/10.3390/ma16020639

Academic Editors: Evgeny Parfenov and Elena Korznikova

Received: 5 December 2022
Revised: 29 December 2022
Accepted: 5 January 2023
Published: 9 January 2023

Copyright: © 2023 by the authors. Licensee MDPI, Basel, Switzerland. This article is an open access article distributed under the terms and conditions of the Creative Commons Attribution (CC BY) license (https://creativecommons.org/licenses/by/4.0/).

1. Introduction

Photocatalysis is capable of harnessing the energy from sunlight, being a solution to many green- and energy-related problems facing the world [1,2]. Titanium dioxide (TiO_2), in the anatase phase, is the most representative photocatalyst due to its strong oxidizing power as well as its physical and chemical stability [3–6]. The qualities of TiO_2 have led to its diverse applications in, for example, self-cleaning surfaces, water splitting, disinfection, and air/water purification [7–10].

The trigger of photocatalysis is the absorption of photons, which are trapped by the photocatalyst to generate electron–hole pairs, subsequently inducing chemical reactions at the surface [11]. However, TiO_2 can only respond to photons with energy larger than 3.2 eV, which is ultraviolet (UV) light, which only accounts for approximately 5% in sunlight [12]. This is considered to be one of the critical limitations for efficient photocatalysis. Thus, to date, extending the wavelength range of the photoactivation of TiO_2 photocatalysts toward the visible-light region is a crucial task to enhance the use efficiency of solar energy.

Elemental doping is an effective strategy to increase the visible light sensitivity of TiO_2 [13,14]. Doping can narrow the bandgap of TiO_2 by downshifting the conduction band bottom or introducing new energy levels within the gap [15–19]. Such states, owing to doping ions, can be used to trap electrons or holes to separate carriers from the bands, thus allowing more carriers to successfully diffuse to the surface. Among the diverse doping elements, copper (Cu) is one of the attractive choices for visible-light harvesting and increased photocatalytic efficiency [20–25]. Although the experimental evidence for

the enhancement in photocatalytic activity in TiO_2 through copper doping is inconclusive, copper doping can modify the large bandgap of TiO_2 to optimize its optical properties for visible-light harvesting. Mingmongkol et al. doped TiO_2 with Cu ranging from 0.1 to 1.0 wt.%, which resulted in the bandgap decreasing from 3.20 eV for undoped TiO_2 to 3.12 eV for 1.0 wt.% Cu-doped TiO_2 [26]. Mathew et al. reported that the visible light absorption property of Cu-TiO_2 increased and the band gap reduced to 2.8 eV with 0.5 mol% Cu [23]. The results of density functional theory (DFT) studies suggested that the introduction of Cu^+ and Cu^{2+} ions creates oxygen vacancies by replacing Ti^{4+} ions in the TiO_2 lattice. The enhancement in photocatalytic activity owing to doping Cu is driven by reduced charge carrier recombination in Cu-TiO_2. Cu dopants (Cu^0, Cu^+, Cu^{2+}) can create multiple bands to extend electron–hole (e^-, h^+) pair recombination; therefore, Cu-TiO_2 exhibits improved electron–hole separation with photoexcitation, resulting in the increase in photocatalytic efficiency [27,28]. The purposes of doping Cu into TiO_2 photocatalyst are: (i) modifying its large bandgap and electronic structure to optimize its optical properties for visible-light harvesting; (ii) improving each step in the charge kinetics to reduce the massive recombination of photogenerated carriers. Photocatalytic activity is optimized at Cu dopant levels between 0.1 and 2 atm.% [27–30]. Above a certain threshold, increasing the Cu dopant concentration diminishes photocatalytic activity through a combination of enhanced recombination and shading [28,30]. The diversity in the reported behavior of Cu dopants and their effects on photocatalytic activity seem to largely stem from diverse materials synthesis methods that result in Cu dopants in nonequilibrium sites as well as from the diverse approaches through which photocatalytic activity is assessed.

Cu has been added to TiO_2 in different mole percentages for various photocatalytic applications such as hydrogen production, CO_2 reduction, decomposition of organic contaminants, and antibacterial/bacterial killing [20–25]. Golon et al. synthesized Cu-TiO_2 via a sol gel method; the doped sample, which was calcined at 600 °C, displayed high photocatalytic activity for phenol degradation [25]. In another study, the gel of Ti(IV) isopropoxide and Cu nitrate was nucleated for 12 h in the dark, the mass was then dried in an oven at 100 °C for 4 h, and the resulting solid mass was finally crushed and calcined at 500 °C for 3 h [31]. Among all the photocatalysts examined in the study, the sample with the lowest Cu concentration produced the most CH_4 (1081 μL h^{-1} g^{-1}) and the highest doping showed the least activity (200 μL h^{-1} g^{-1}) under similar conditions. In most cases, the synthesis procedures require high-temperature calcination, so are not suitable for forming photocatalyst films on the platforms of technologically important substrates such as plastics and glasses. Another attractive approach to synthesize Cu-doped nanocrystalline TiO_2 is the hydrothermal method; this method can be employed under self-produced pressures at low temperatures [32,33]. Typically, the precursor solution is transferred to a Teflon-lined stainless-steel autoclave and heated at ~180 °C for 12 h. The operating temperature is above the melting point of plastics, and the pressure inside a reactor is known to be in the mega pascals range; therefore, this technique is incompatible with forming a film on a flexible substrate such as plastics [34]. The precipitation method was used to synthesize Cu-doped nanocrystalline TiO_2; this method can be performed using low-cost materials and easier manufacturing methods at industrial scales. Recently, A.M. Alotaibi et al. used aerosol-assisted chemical vapor deposition (AACVD) to deposit highly photoactive thin films of Cu-doped anatase TiO_2 on glass substrates [22]. In their study, a solution of titanium isopropoxide, copper nitrate, and ethyl acetate was atomized using a piezoelectric device, and the generating aerosol was transferred with N_2 flow onto the glass substrate heated at 470 °C. AACVD provides a facile route for producing highly photoactive Cu-doped TiO_2 thin films. In such films, the interactions between substitutional and interstitial Cu in the anatase lattice can explain the extended exciton lifetimes and the enhanced photocatalytic and antibacterial ability. Thus, although many researchers have focused on the preparation of Cu-TiO_2 using sol–gel and hydrothermal techniques, studies on synthesis or coating techniques with operation at low temperatures or under normal pressure are scarce.

In this context, in this study, we aimed at producing Cu-TiO_2 structures at low temperature (<~80 °C). For this, we employed the liquid phase deposition (LPD) technique as a method to produce TiO_2 nanostructures. LPD is a simple and economical approach to generate TiO_2 with an anatase phase at room temperature, which was first reported by Deki in 1996 [35]. LPD synthesis is based on the hydrolysis of ammonium hexafluoro titanate [$(NH_4)_2TiF_6$], with boric acid used as the fluorine ion scavenger, forming TiO_2 via a ligand exchange reaction [35,36]. As this reaction proceeds at room temperature and atmospheric pressure, LPD is applicable for non-heat-resistant materials such as polystyrene, glass, etc. [37–39]. In this study, based on the LPD technique, we dissolved Cu salts into a precursor solution for Cu doping, after which we microscopically and spectroscopically characterized the products to prove the possibility of controlling the Cu-doping level.

2. Materials and Methods

2.1. Sample Preparation

Following the typical LPD procedure described in a previous study [39], we produced TiO_2 samples through a temperature-assisted liquid phase deposition process, whose procedure is schematically illustrated in Figure 1. For the precursors, we used $(NH_4)_2TiF_6$ (AHFT) (FUJIFILM Wako, 1st Grade) and H_3BO_3 (FUJIFILM Wako, 1st Grade). We separately dissolved both materials in distilled water at 0.1 M and 0.3 M for AHFT and boric acid, respectively. This ratio allowed the production of the anatase phase of TiO_2. For doping copper ions, we then mixed the solutions with several types of Cu salts under vigorous stirring for 15 min. Here, as Cu salts, we applied $Cu(NO_3)_2{\cdot}3H_2O$ (FUJIFILM Wako, Wako Special Grade), $CuCl_2$ (Kojundo Chemical Laboratory Co., Ltd., Tokyo, Japan), and $Cu(CH_3COO)_2$ (FUJIFILM Wako, Wako Special Grade). Next, we fixed a glass substrate (50 × 50 mm) in a beaker so that the coating surface was kept downward to avoid particle deposition on this surface, which we then placed in an oven at 70 °C for 3 h. In a previous study, a temperature of 70 °C and a reaction time of 3 h was favorable for improved crystallinity and photocatalysis. Prior to use, we thoroughly cleaned the glass substrates by ultra-sonication in acetone (99%) and performed hydrophilic treatment with a table-top UV/Ozone Processor (SSP16-110, SEN LIGHTS). We changed the concentration of Cu salts up to 10 mM for producing different doping levels. Here, we did not apply doping levels higher than 10 mM to avoid excess doping, which weakens photocatalytic activity. After the reaction proceeded for 3 h, we removed the substrate, which we rinsed in distilled water and dried with a blower. We obtained the powders after separation by centrifugation (3500 rpm) for 15 min, which we washed by dispersion in distilled water, centrifuged three times, and then dried at room temperature.

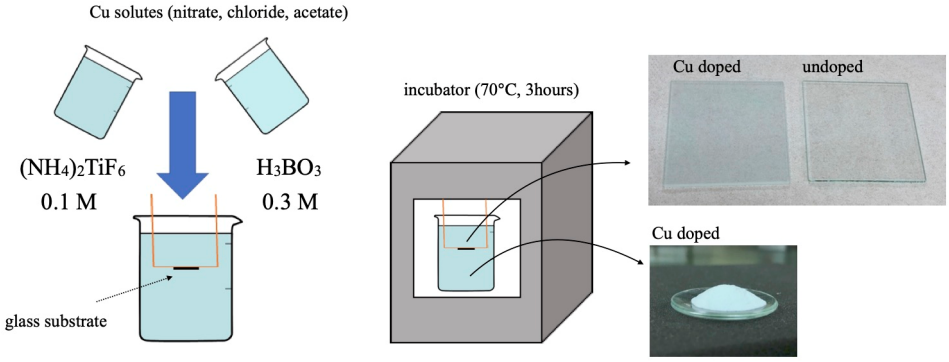


Figure 1. Schematic illustration of experimental procedure for producing Cu-doped TiO_2 powders and coatings via liquid phase deposition.

2.2. Characterization

We characterized the substrate samples with a Raman spectroscope (NRS-3300, JASCO), UV–vis spectrometry (UV mini 1240, Shimadzu), a scanning electron microscope (SEM)

(JSM-7800F, JEOL), an electron probe micro-analyzer (EPMA) (JXA-8530F, JEOL), and X-ray photoelectron spectroscopy (XPS) (PHI5000 VersaProbe, ULVAC-PHI Inc.). We determined the optical band gap of the nanoparticles using diffuse reflection spectroscopy (DRS) with a fiber optic reflectance sphere (#58-583, Edmund OPTICS). We calculated the band gap energies using the Kubelka−Munk (K-M) method based on the diffuse reflectance spectra, where $F(R) = (1 - R)^2/2R$ [40].

2.3. Photocatalysis

We observed the photocatalytic activity of the Cu-TiO_2 substrate through decomposing acetaldehyde gas. We performed the photocatalysis experiment based on a JIS R1701-2. We tested powder products for action spectral measurement through the degradation of methylene blue (MB, Nacalai Tesque, Inc., Nakagyo-ku, Kyoto, Japan) as a model organic compound. We prepared the solution for a reaction by adding 25 mg of the sample into 50 mL of 10 ppm MB solution in a glass beaker, which we then mixed via ultrasonication for several minutes. We initiated the photocatalytic reactions with xenon lamp (MAX505, Asahi Spectra) illumination, where we extracted the specific wavelength (320, 360, 400, 440, 480, and 520 nm) by using bandpass filters for action spectral measurement. During the reaction, we continuously stirred the solution with a magnetic stirrer at 300 rpm. After extracting the MB solution via centrifugation, we monitored the time-dependent decay of MB absorbance centered at 665 nm after 30, 60, 90, and 120 min of irradiation using a UV–Visible Spectrophotometer (Shimadzu UV mini-1240).

3. Results and Discussion

3.1. Choice of Cu Salts for Doping

Figure 2 presents the SEM images of undoped and doped samples prepared with different types of Cu salt: $Cu(NO_3)_2{\cdot}3H_2O$, $CuCl_2$, $CuSO_4{\cdot}5H_2O$, or $Cu(CH_3COO)_2$. In these experiments, we fixed the concentration of these salts at 10 mM. Most of the products had waxberry-like structures; in Figure 2, the size increased when using Cu salts. Among several types of Cu salts, the products with Cu acetate exhibited fewer protrusions, which was due to the inhibition of crystal growth. In addition, this morphology suggests poor photocatalytic activity due to is small surface area. Thus, crystal growth should be improved with the use of Cu nitrate or chloride, whereas Cu acetate is less effective in terms of forming fine structures.

To further understand the molecular vibrational state, we applied Raman spectroscopy. Figure 3 shows the Raman spectra of undoped and doped samples prepared with different types of Cu salt (10 mM). We assigned the Raman peaks at 152, 404, 513, and 634 cm^{-1} to the E_g, B_{1g}, A_{1g}, and E_g modes of the anatase phase, respectively [39,41]. The strongest E_g vibrational mode (at 152 cm^{-1}) seen in all samples was caused by symmetric O-Ti-O stretching vibrations in TiO_2, indicating the formation of an anatase phase in the LPD process even with dissolving Cu salts in a precursor solution. The XRD patterns also confirmed the crystallographic nature of anatase TiO_2, whereas the doped samples exhibited poor crystallinity comparing with the undoped ones (Figure S1). Based on the Scherrer equation, we calculated the crystallite size of undoped TiO_2 to be ~50 nm; doped TiO_2 is expected to be smaller according to the wide FWHM values [39,42]. Analyzing the XRD patterns of doped samples is difficult due to spectral noise; therefore, we performed curve-fittings in E_g Raman mode to evaluate the local structure of TiO_2. Table 1 shows that the FWHM values increased with the addition of copper chloride and copper acetate; only the copper nitrate precursor solution had an FWHM value comparable to that of the undoped TiO_2. These FWHM values could be explained by the structure of crystals. In general, the spectral line shape of crystal lattice vibrations (or phonons) is inversely proportional to the lifetime of the phonons [43]. In the case of an ideal harmonic crystal, the line shape is infinitesimally narrow. Experimental evidence shows that the Raman line always has a finite width, indicative of the presence of phonon-vibrational decay. The broadening of the Raman line width is attributed to the phonon scattering (decay) owing

to the presence of impurities and/or defect sites and crystallite edges in the crystallites. Therefore, in our experiments, we expected the use of copper chloride and acetate to induce lattice disorders or size reduction to generate more impurities and/or defect sites and crystallite edges. However, copper nitrate, as shown in Table 1, produced fewer effects that hindered the atomic arrangement, resulting in maintaining the crystallinity of the products. Therefore, we concluded the use of Cu nitrate is more appropriate for Cu doping into TiO_2 with LPD process from the viewpoint of improved crystallinity, which may enable efficient photocatalysis.

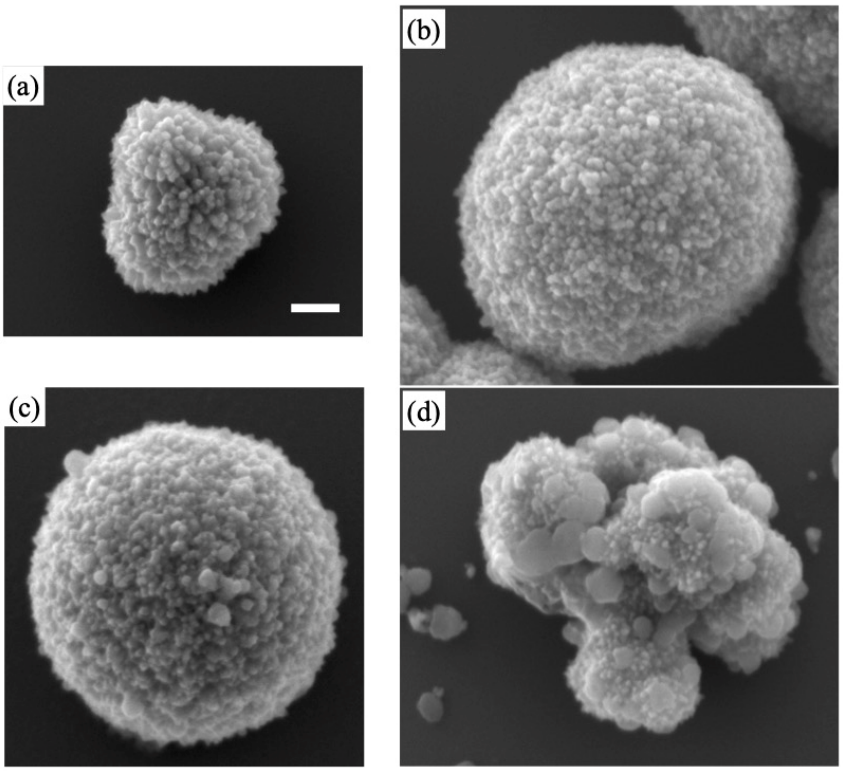


Figure 2. SEM images of (**a**) undoped and (**b**,**d**) Cu-doped TiO_2 particles (10 mM): (**b**–**d**) nitrate, chloride, and acetate, respectively. Scale bar indicates 200 nm.

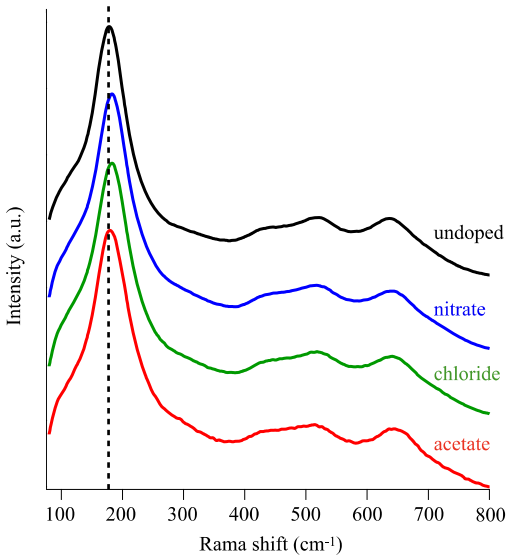


Figure 3. Raman spectra of undoped (black) TiO_2 and TiO_2 doped with nitrate (blue), chloride (green), and acetate (red). The spectral intensity was normalized.

Table 1. Dependence of FWHM values on Cu salt species.

Solute	FWHM (cm^{-1})
-	30.2
$Cu(NO_3)_2$	30.0
$CuCl_2$	31.8
$Cu(CH_3COO)_2$	34.5

3.2. Concentration Dependence on Crystal Structures

We changed the concentration of Cu nitrate from 0.1 to 10 mM, and we observed the morphology of the powder products and coatings by SEM. Figures 4a–c and 5a–d show SEM images of the powder and coating samples prepared with different concentrations of Cu nitrate (0.1, 1.0, and 10 mM). The size histogram measured with SEM is shown in Figure 6. The size of the particles was 1.4–1.5 μm, on average, for 0.1 and 1.0 mM. However, the particle size decreased as the concentration increased up to 10 mM. This was likely due to the excess doping, which inhibited crystallization.

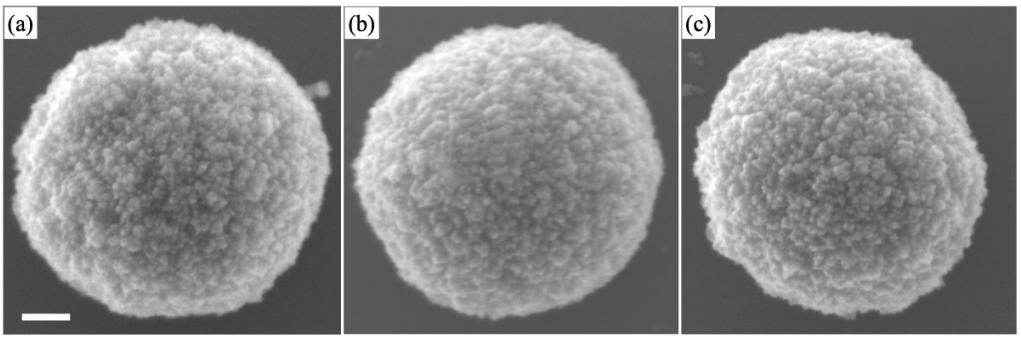


Figure 4. SEM images of Cu-doped TiO_2 particles with different dopant concentrations: (**a**) 0.1, (**b**) 1, and (**c**) 10 mM. Scale bar indicates 200 nm.

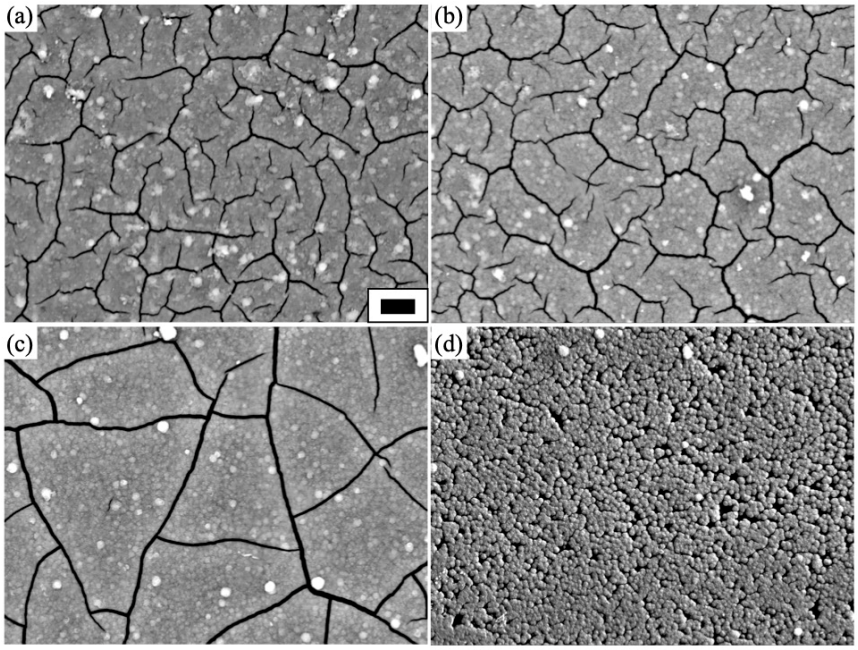


Figure 5. SEM images of Cu-doped TiO_2 coatings with different dopant concentrations: (**a**) 0, (**b**) 0.1, (**c**) 1, and (**d**) 10 mM. Scale bar indicates 2 μm.

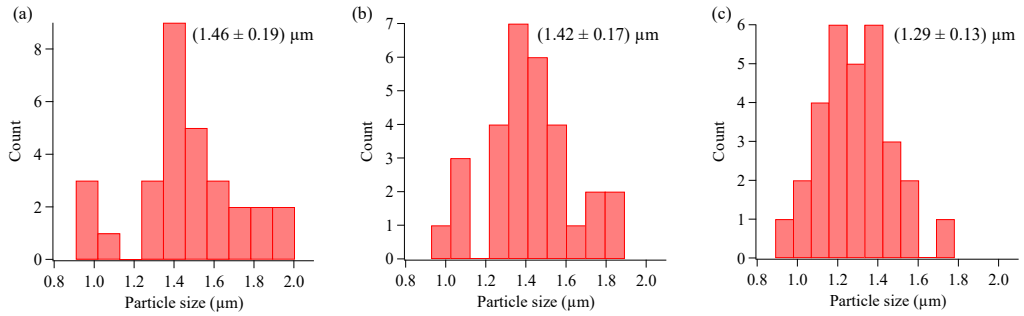


Figure 6. Size distribution of particles prepared with different concentrations of Cu nitrate: (**a**) 0.1, (**b**) 1, and (**c**) 10 mM.

For the coatings, we observed plate-like structures with large cracks between the plates on the glass substrate. The formation of large cracks between plates is an often-observed phenomenon when forming thick films [44]. The surface texture of a plate seemed to be smooth with the absence of protrusions, which considerably differed from that of the powder sample. We think this was caused by crystal growth from densely distributed nuclei. In the LPD process, nucleation starts from the hydroxyl groups, which act as nucleation sites. Without hydrophilization treatment of the substrate, we observed the decrease in density of nucleation sites, generating a waxberry-like structure with a sparse distribution (Figure S2).

We found that the change in Cu concentration affected the surface morphology of the Cu-TiO_2 coatings, as shown in Figure 5b–d. The plate grew larger as the concentration increased from 0.1 to 1.0 mM. When we applied 10 mM, a granular structure formed, and plate-like structures did not form. We expected the addition of Cu ions into the precursor solution to enhance the crystallization to generate larger plates, which we observed for the produced powder samples (Figure 2). However, at the higher concentration (10 mM), plate-like structures and cracks were absent. The absence of cracks was due to the inhibition of nucleation and further crystal growth by the copper dopants dissolved in the solution. For the synthesis of TiO_2 thin films, we employed an aqueous solution of ammonium hexafluoro titanate ($(NH_4)_2TiF_6$) and boric acid (H_3BO_3) as the titanium fluoride complex and F^- scavenger, respectively. The titanium fluoride complex is hydrolyzed to titanium hydroxide and free F^- ions. The produced F^- ions can then be scavenged by H_3BO_3 [35,36,39]. The hydroxyl groups at the surface of a glass substrate induce hydrolyzation to form TiO_2 films. When Cu nitrate is dissolved in a solution, Cu^{2+} is subject to diffusion over the hydroxylated surface [45]. Therefore, the diffusion of Cu ions over a hydroxylated surface is expected to diminish the hydrolysis (ligand-exchange) reaction of titanium fluoride complexes, resulting in a reduction in the density of TiO_2 particles. The particles are isolated; therefore, less agglomeration occurs, so the cracks disappear.

Figure 7a,b represent the Raman spectra of powder and coating samples, respectively. Through the comparison of the spectral patterns in Figure 7a, we found that all samples were anatase-phase TiO_2. Despite the weak peaks in the coating samples, as shown in Figure 7b, the presence of the principal E_g vibrational mode (at 155 cm^{-1}) suggested the formation of anatase TiO_2 on a substrate. Notably, the spectral width (FWHM) and peak wavenumber should be dependent on the Cu doping concentration.

Figure 8a,b depict the dependence of peak wavenumber and FWHM values on the concentration of Cu nitrate, respectively. In both the coating and powder cases, the strongest E_g peak blue-shifted as the Cu concentration increased from 0.1 to 10 mM. The blue shift in the E_g vibrational mode probably occurred due to the substitution of smaller Ti cations (0.605 Å) by larger Cu cations (0.73 Å). As larger Cu^{2+} ions replace smaller 4+ ones in their position, anatase TiO_2 crystal is expected to be subject to compressive stress [46]. With higher doping concentrations, we observed a monotonical increase in the FWHM values of the E_g vibrational mode. The replacement of Cu by Ti ions was expected to induce disarrangement of Ti-O networks, which would result in the lower crystallinity of the products.

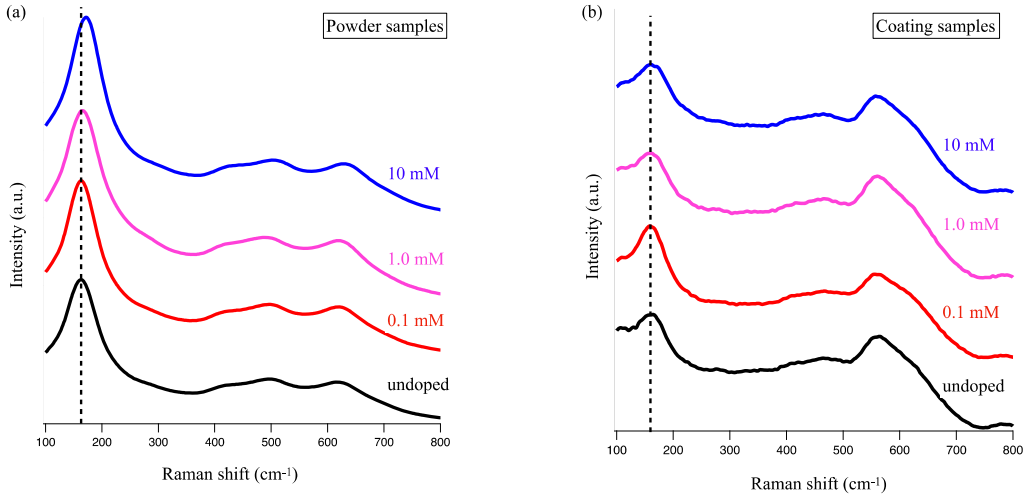


Figure 7. Raman spectra of Cu-TiO_2 (**a**) powder and (**b**) coating samples. Black line indicates undoped TiO_2. Red, pink, and blue lines correspond to Cu concentrations of 0.1, 1.0, and 10 mM, respectively.

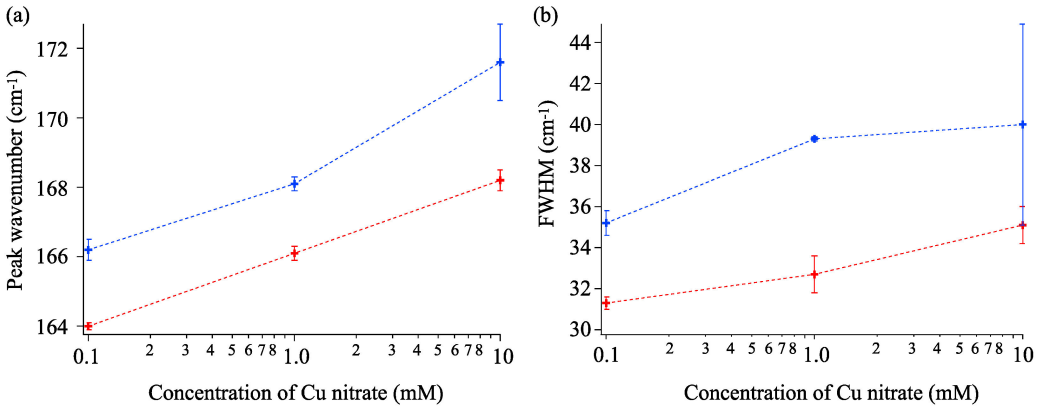


Figure 8. Concentration dependence on (**a**) peak wavenumber of Raman E_g mode and (**b**) spectral width. Red and blue indicate coating and powder samples, respectively.

The EDS and EPMA elemental mapping images for undoped and Cu doped samples are presented in Figures 9 and 10, respectively, which demonstrate that all the three elements (Ti, O, and Cu) were uniformly distributed in both the doped powder and coating samples. Thus, using LPD enables the preparation of doped TiO_2 nanomaterials with a homogeneous distribution of doping ions.

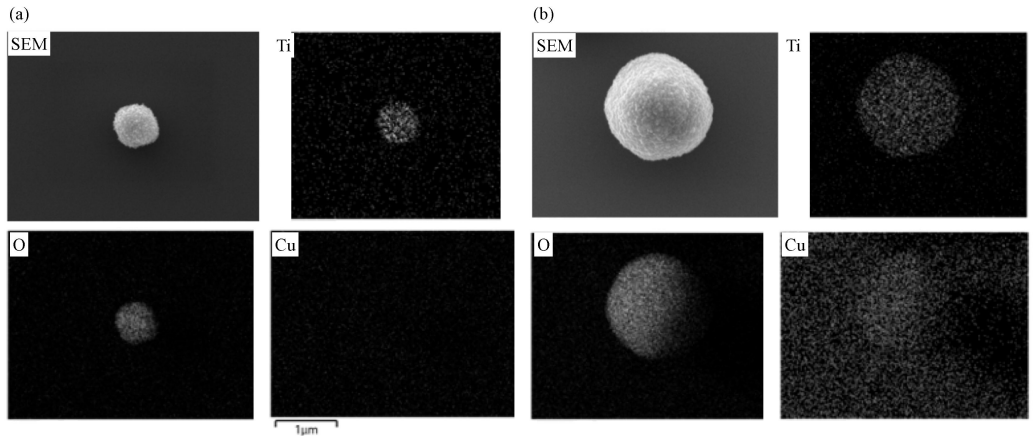


Figure 9. SEM and EDS mapping of (**a**) undoped and (**b**) Cu doped TiO_2. Cu nitrate concentration was 10 mM.

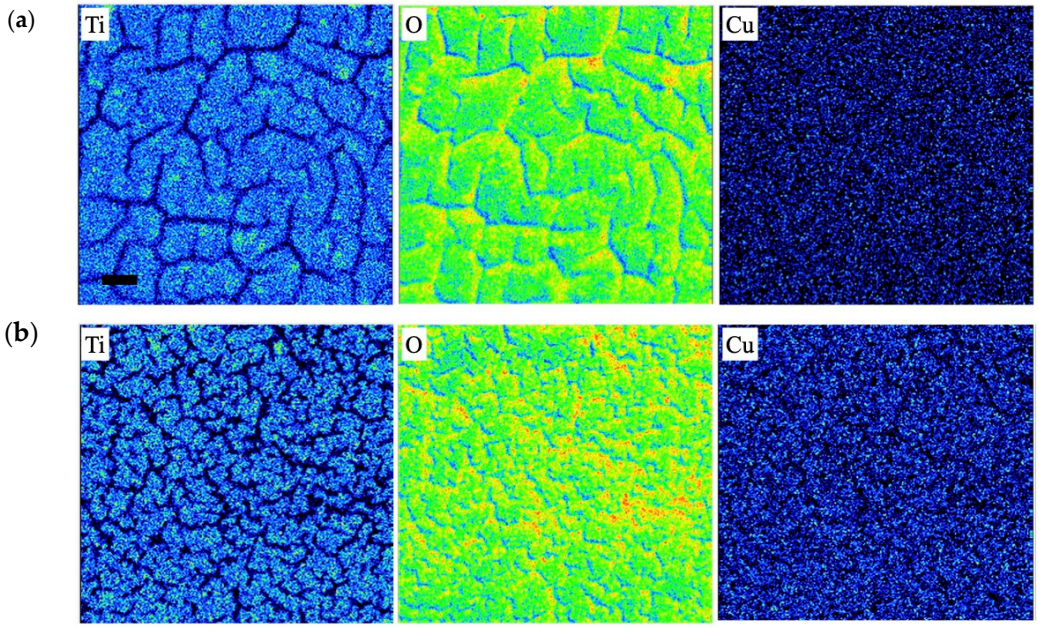


Figure 10. Elemental mapping of (**a**) undoped and (**b**) Cu doped TiO_2 coated on glass substrate. Cu nitrate concentration was 10 mM.

3.3. Doping Levels and Optical Properties

We measured the atomic concentration of Cu in the powder and coating samples with EDS and EPMA; the results are shown in Figure 11. With increasing Cu nitrate concentration from 0 to 10 mM, the atomic concentration changed from 0 to 0.8 and 1.3 atm.% in the powder and coating samples, respectively.

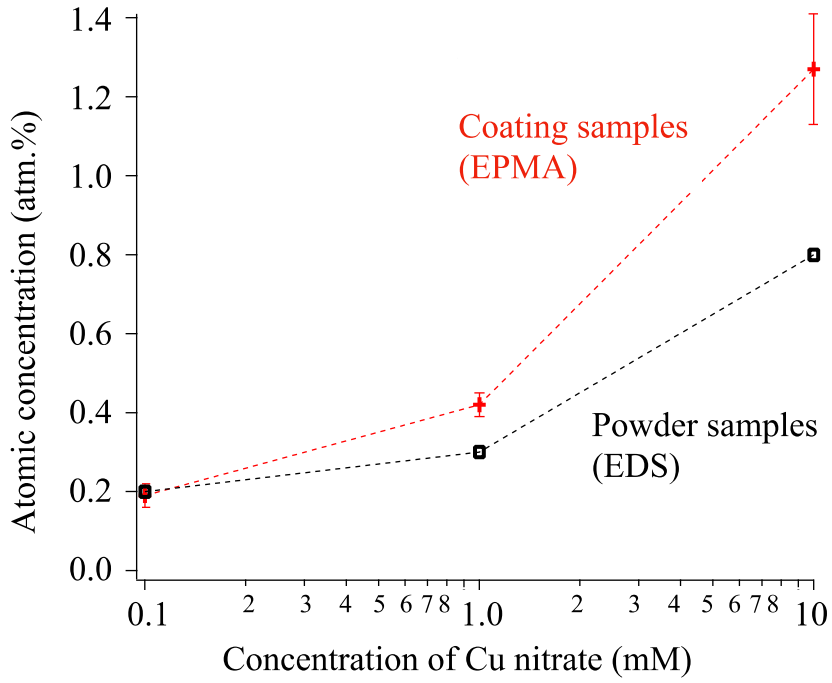


Figure 11. Atomic concentration of Cu incorporated into powder and coating samples.

Figure 12 presents the Kubelka–Munk (K–M) plots we obtained through diffusion reflectance measurements for the samples without (black) and with Cu doping (red, pink, and blue). We determined the bandgap of the material by extrapolating the linear part of $[F(R)*h\nu]^{1/2}$ to zero when plotted against E(hν,) as shown in Figure 12. (see Table 2) The

bandgap of undoped TiO_2 powders is shown in Figure 12 at 3.30 eV, which was slightly larger than that of bulk TiO_2 with an anatase phase (3.2 eV) [47]. As the crystallite size of the doped samples was less than 50 nm, the larger bandgap observed here might have been due to the particle size effect [48–50]. The subgap region showed an Urbach-like tail at 3.10–3.25 eV. This indicated a distribution of shallow states just below the conduction band minimum (CVM), though the origin of shallow gap states is still unclear [51]. When we applied 0.1 mM Cu nitrate, the bandgap remained at 3.30 eV; the tail observed with undoped TiO_2 was invisible in the pink spectrum. The absence of the tail indicated less disorder (e.g., oxygen vacancy) formed in the TiO_2 lattice, which agreed well with the results of SEM observation (Figure 5), Raman spectroscopy (Figure 8), and XRD analysis (Figure S1). In this case, with a single compensating oxygen vacancy, the empty 3d state of the Cu^{2+} ions lies above the CBM of the TiO_2 host, so that the dopant does not impact the magnitude of the bandgap. With higher levels of Cu doping (1.0 and 10.0 mM), we observed two features, as shown in Figure 12: (i) red-shifting of the band originating from TiO_2; (ii) creating additional states just below the original band. The red-shift of the bandgap to 3.15 eV (1.0 mM) and 2.90 eV (10.0 mM) could be explained by the coexistence of Cu^{2+} ions and oxygen vacancies. Mathew et al. studied the electronic states of Cu-TiO_2 based on the density functional theory simulation, in which the introduction of Cu^{+} and Cu^{2+} ions by replacing Ti^{4+} ions in the TiO_2 lattice created oxygen vacancies to extend the valence band maximum (VBM). Contrary to the case with 0.1 mM, Cu-derived states emerged between the valence band edge and extended the VBM to higher energies, leading to a decrease in the band gap. In addition, gap states were created between the VBM and CBM, which was evident as the presence of an absorption tail ranging from 3.05 to 3.25 eV for 1.0 mM and from 2.50 to 3.20 eV for 10.0 mM Cu nitrate. Cu-TiO_2 with 10 mM Cu nitrate exhibited optical response in the visible region (wavelengths shorter than 430 nm), which is beneficial for the efficient use of solar light for photocatalysis.

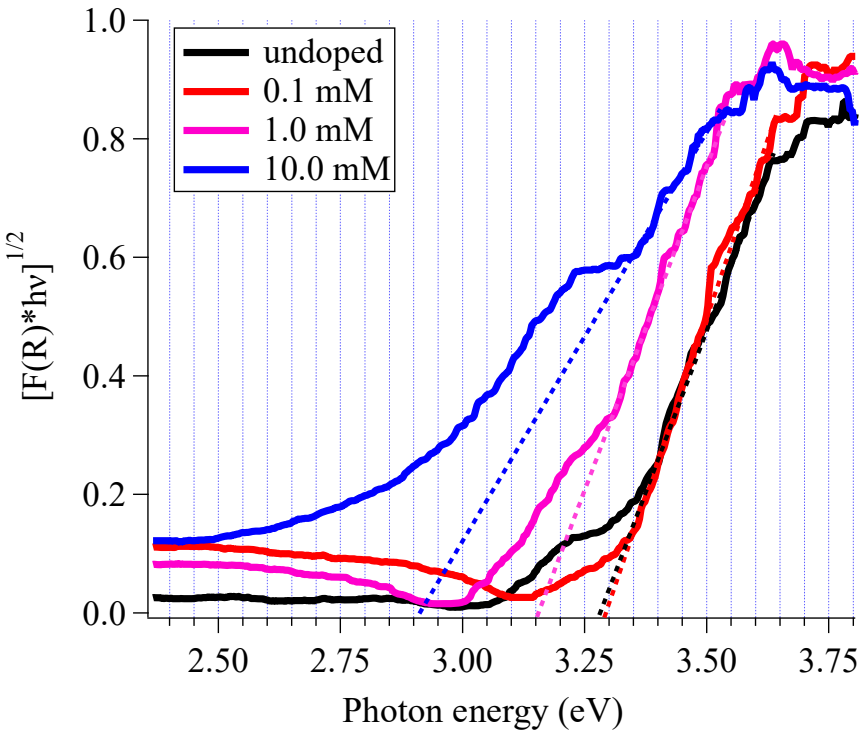


Figure 12. Tauc plots of samples prepared with 0 (black), 0.1 (red), 1.0 (pink), and 1.0 (blue) mM Cu nitrate.

Table 2. Concentration dependence on atomic concentration of Cu and bandgaps.

Conc. (mM)	Atm.%	Bandgap (eV)
0.0	0.0	3.30
0.1	0.2	3.30
1.0	0.4	3.15
10	1.3	2.90

3.4. XPS Analysis

Figure 13 presents the XPS spectra of coating samples synthesized with 10 mM Cu nitrate. Figure 13a,b indicate the narrow scans for Ti 2p and Cu 2p, respectively. We fitted the XPS data to highlight the peak position and FWHM values, which are summarized in Table S1. The fitted curves are presented as dotted curves in Figure 13. We attributed the two strong symmetrical peaks at around 464.1 and 458.4 eV to Ti $2p_{1/2}$ and Ti $2p_{3/2}$, respectively. The peak separation of 5.7 eV shown in the Ti 2p doublet agrees well with the energy reported for TiO_2 nanoparticles with an anatase phase [52]. Those peaks were 1.1 eV lower than those in anatase TiO_2, which is generally caused by the presence of a higher anionic vacancy. The peak of the Ti $2p_{3/2}$ spectrum located between Ti^{4+} (459.2 eV) and Ti^{3+} (457.5 eV) [53]; however, we could not obtain a good fit with two components of Ti^{4+} and Ti^{3+}, potentially due to the complex defect states of Cu/O vacancies. The Cu2p spectrum on deconvolution exhibited an intense peak at 932.4 eV and a shorter peak at 931.7 eV, which we ascribed to the Cu^{2+} and Cu^{+} states, respectively [31]. The absence of the satellite peak (942.6 eV) suggested that the Cu was doped in the TiO_2 anatase lattice and did not form a surface CuO layer [54]. The doped Cu existing in oxidation state of Cu^{+} resulted in the formation of single oxygen vacancies. However, we did not observe the signal corresponding to Ti^{3+} sites in the Ti 2p region, potentially because that the Cu dopant present in the TiO_2 lattice as either Cu^{2+}/Cu^{+} had lower valency and higher electronegativity compared with those of Ti^{4+}. To conserve the lattice charge as a result of the incorporation of aliovalent Cu ions in the anatase TiO_2 matrix, ionic vacancies (O vacancies) in several sites may have formed.

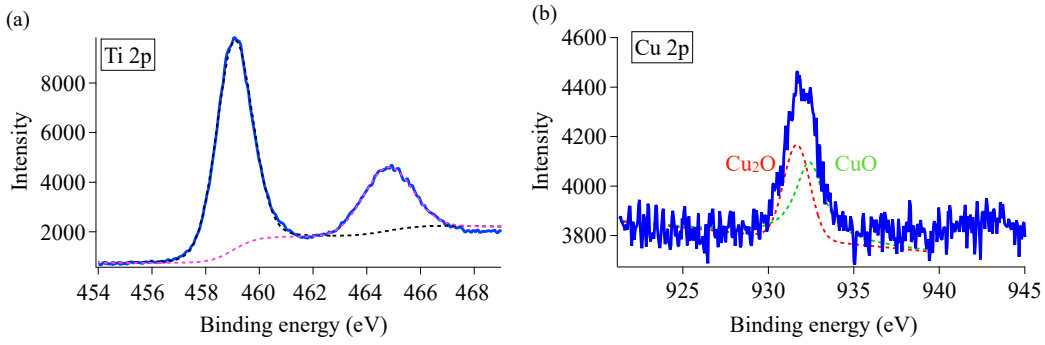


Figure 13. XPS spectra of Cu-doped TiO_2 prepared with 10 mM Cu nitrate. (**a**,**b**) Narrow scans for Ti 2p and Cu 2p, respectively. (**b**) Green, red, and gray lines indicate Cu_2O, CuO, and $Cu(NO_3)_2$, respectively.

3.5. Photocatalysis

We observed the photocatalytic activity of undoped and Cu doped TiO_2 through decomposing acetaldehyde gas into CO_2 and H_2O. Figure 14 shows the concentration decay of acetaldehyde with light irradiation. In all cases, we confirmed the reduction of acetaldehyde gas and generation of CO_2 (Figure S3) gas. Cu-TiO_2 with 0.1 and 1.0 mM Cu nitrate exhibited a higher rate of reaction, whereas we found lower activity for the sample with 10 mM Cu nitrate doping. We calculated the average rate constants and standard deviations for undoped and Cu-doped TiO_2, and the obtained values are summarized in Table 3. The

Cu doping through the LPD process is described in Table 3, which increased photocatalytic efficiency (1.3 times). The undoped TiO_2 prepared via LPD exhibited considerable MB degradation activity, as confirmed by a photocatalytic activity 3–4 times higher than that of the commercial photocatalyst P25-Degussa in our previous study [39]. Therefore, the photocatalytic activity of Cu-TiO_2 in this study should be 4–5 times higher than that of the commercial photocatalyst P25-Degussa. Enhanced activity is most often driven by reduced charge carrier recombination in Cu-TiO_2 materials [27,28]. This arises as the result of photo-generated electrons facilitating the reduction $Cu^{2+} + e^- \rightarrow Cu^+$, thus extending the valence band hole lifetimes at surfaces, which are able to react with adsorbed species to form active radicals. In our case, the results of XPS analysis confirmed the presence of Cu^{2+}. The results of the Raman study and XRD analysis confirmed the absence of Cu_2O structures. These results do not necessarily preclude the existence of amorphous or fine secondary oxide precipitates, which may improve exciton lifetime through electron capture in the secondary phase or enhance activity through an increased surface area [55–57]. The contribution of the mechanism discussed above was dominant in the 0.1 mM doped Cu-TiO_2; an improvement in the light absorption of TiO_2 resulted in the promotion of photocatalysis in the 1.0 and 10.0 mM cases. The light absorption edge extended to 3.15 and 2.90 eV for each sample, as shown in the K-M plots (Figure 12 and Table 2).

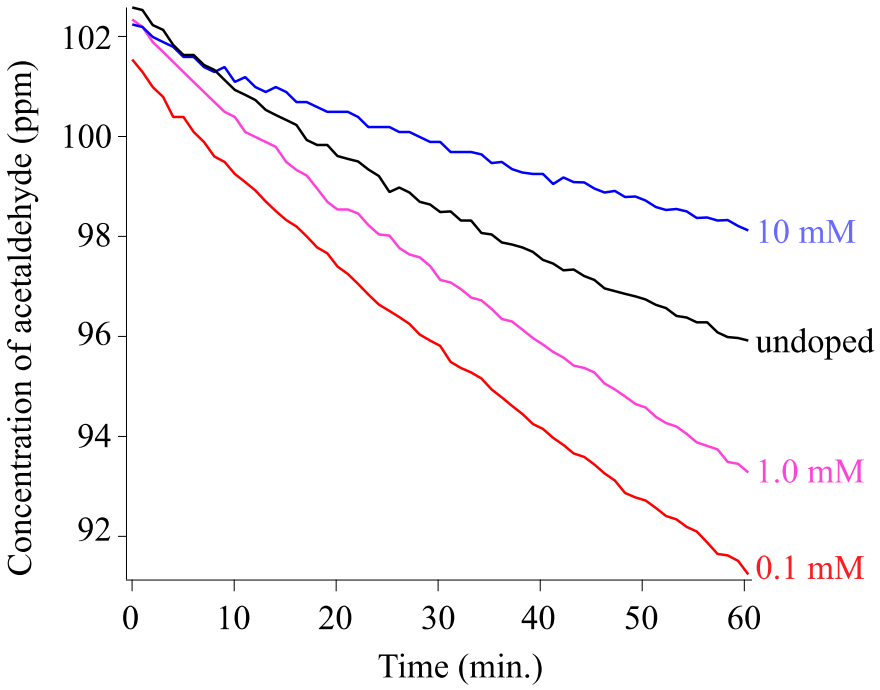


Figure 14. Photocatalytic decomposition of acetaldehyde by undoped (black) and Cu doped TiO_2 (colors) coated on a glass substrate. Red, pink, and blue curves denote 0.1, 1.0, and 10.0 mM Cu nitrate used for synthesis, respectively.

Table 3. Average rate constant for undoped TiO_2 and Cu-TiO_2.

Cu Nitrate (mM)	Rate Constant *k* (ppm/min.)	Std. Error (ppm/min.)
0.0	0.00131	0.00025
0.1	0.00164	0.00011
1.0	0.00156	0.00012
10	0.00068	0.00006

To reveal the contribution of the response in the visible light region, we evaluated the action spectra of Cu-TiO_2 (10.0 mM). Figure 15 shows the light absorption and action spectrum of Cu-TiO_2. Here, we applied 10 mM Cu nitrate, and we performed further annealing treatment to easily observe photocatalytic reaction. As shown in Figure 15, the action spectrum confirmed that the decomposition of MB occurred with 440 ± 10 nm or shorter wavelengths (corresponding to 2.76–2.88 eV energy). Thus, the Cu-TiO_2 produced in our experiments responded to visible light to induce photocatalysis, which agrees with the bandgaps shown in Figure 12.

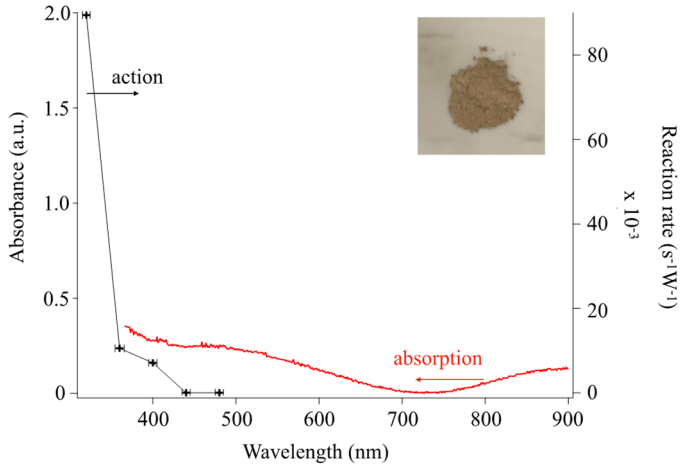


Figure 15. Action and absorption spectrum of Cu-TiO_2 prepared with 10.0 mM of Cu nitrate. Thermal treatment under nitrogen for 1 h was performed after synthesis. Inset shows photograph of doped sample.

4. Conclusions

In this study, we found that after properly choosing a Cu dopant source for crystal growth, liquid phase deposition could be used produce Cu-doped TiO_2 at low operating temperatures (around 70 °C) under atmospheric pressure, with a controllable level of incorporated ions. We dissolved several different types of Cu salts in a precursor solution as a source of Cu ions; we found that Cu nitrate was the best choice for generating Cu-doped TiO_2 with improved crystallinity. The results of Raman spectroscopy revealed the formation of anatase TiO_2 in all samples with and without Cu ion doping. Based on the SEM measurements, we observed that the structure of the powder samples was micron-sized particles with a waxberry-like structure, which maintained their structure after increasing the Cu nitrate concentration up to 10 mM. The coating samples produced with less than 1.0 mM displayed plate-like structure with cracks, whereas we found individually distributed particles by increasing the doping concentration to 10.0 mM. We think the plate-like structure formed due to the crystal growth from densely distributed nuclei. Additionally, excess doping of Cu ions inhibited the nucleation on the substrate to reduce the density of TiO_2 particles, resulting in the disappearance of plates and cracks. The results of elemental mapping revealed the homogeneous distribution of Cu atoms across the doped particles and coatings, and we could control the doping level of Cu cations up to ~1.4 atm.% when we applied 10 mM $Cu(NO_3)_2$. Based on the results of the Raman and XPS studies, we concluded that the Cu ions were incorporated in the lattice of TiO_2 in the Cu^+ or Cu^{2+} states, which resulted in a slight shrinkage of the cell of the produced material. Finally, we enhanced the photocatalytic performance through decomposing acetaldehyde gas on Cu-TiO_2 coating samples, which could be explained by their more efficient light absorption in the visible region or the efficient carrier diffusion in the products. Above a certain threshold (1.0 mM doping), increasing the Cu dopant concentration diminished the photocatalytic activity. We found that improvements in photocatalytic activity were optimized at Cu dopant levels between 0.2 and 0.4 atm.%. This approach is potentially

applicable for coating visible light photocatalysts onto a technologically important substrate with a low melting-point, such as glass substrates, plastics, and polymers.

Supplementary Materials: The following supporting information can be downloaded at: https://www.mdpi.com/article/10.3390/ma16020639/s1, Figure S1: XRD patterns of undoped (black) and Cu-doped TiO_2 (colors). In panel (a), different copper salts, nitrate, chloride, and acetate are denoted by blue, green, and red, respectively. In panel (b), red, pink, and blue colors indicate different concentrations, 0.1, 1.0 and 10.0 mM, respectively.; Figure S2: SEM images of TiO_2 coated on a glass substrate (a) with and (b) without hydrophilization treatment by UV illumination; Figure S3: Production of CO_2 during the decomposition of acetaldehyde. Table S1: Peak positions and FWHM values obtained by fitting XPS data.

Author Contributions: M.H.: Conceptualization, Methodology, Data Analysis, and Writing. T.O.: Editing and Photocatalysis Evaluation. P.L.: Sample Preparation and Characterization. Y.Y.: Sample Preparation and Characterization. Y.I.: Supervision and Editing. All authors have read and agreed to the published version of the manuscript.

Funding: This study was financially supported by The Hibi Science Foundation and The Iketani Science and Technology Foundation (0341180-A).

Institutional Review Board Statement: Not applicable.

Data Availability Statement: Not applicable.

Acknowledgments: The Raman spectroscopy, SEM-EDS, and EPMA measurements were supported by the Equipment Sharing Division, Organization for Co-Creation Research and Social Contributions, Nagoya Institute of Technology.

Conflicts of Interest: The authors declare no conflict of interest.

References

1. Fujishima, A.; Zhang, X.; Tryk, D.A. TiO_2 Photocatalysis and Related Surface Phenomena. *Surf. Sci. Rep.* **2008**, *63*, 515–582. [CrossRef]
2. Dhakshinamoorthy, A.; Navalon, S.; Corma, A.; Garcia, H. Photocatalytic CO_2 Reduction by TiO_2 and Related Titanium Containing Solids. *Energy Environ. Sci.* **2012**, *5*, 9217. [CrossRef]
3. Carcel, R.A.; Andronic, L.; Duta, A. Photocatalytic Activity and Stability of TiO_2 and WO_3 Thin Films. *Mater. Charact.* **2012**, *70*, 68–73. [CrossRef]
4. Fujishima, A.; Honda, K. Electrochemical Photolysis of Water at a Semiconductor Electrode. *Nature* **1972**, *238*, 37–38. [CrossRef] [PubMed]
5. Mino, L.; Negri, C.; Santalucia, R.; Cerrato, G.; Spoto, G.; Martra, G. Morphology, Surface Structure and Water Adsorption Properties of TiO_2 Nanoparticles: A Comparison of Different Commercial Samples. *Molecules* **2020**, *25*, 4605. [CrossRef]
6. Augugliaro, V.; Bellardita, M.; Loddo, V.; Palmisano, G.; Palmisano, L.; Yurdakal, S. Overview on Oxidation Mechanisms of Organic Compounds by TiO_2 in Heterogeneous Photocatalysis. *J. Photochem. Photobiol. C Photochem. Rev.* **2012**, *13*, 224–245. [CrossRef]
7. Lonnen, J.; Kilvington, S.; Kehoe, S.C.; Al-Touati, F.; McGuigan, K.G. Solar and Photocatalytic Disinfection of Protozoan, Fungal and Bacterial Microbes in Drinking Water. *Water Res.* **2005**, *39*, 877–883. [CrossRef]
8. Herrmann, J.-M. Heterogeneous Photocatalysis: Fundamentals and Applications to the Removal of Various Types of Aqueous Pollutants. *Catal. Today* **1999**, *53*, 115–129. [CrossRef]
9. Hager, S.; Bauer, R. Heterogeneous Photocatalytic Oxidation of Organics for Air Purification by near UV Irradiated Titanium Dioxide. *Chemosphere* **1999**, *38*, 1549–1559. [CrossRef]
10. Ochiai, T.; Aoki, D.; Saito, H.; Akutsu, Y.; Nagata, M. Analysis of Adsorption and Decomposition of Odour and Tar Components in Tobacco Smoke on Non-Woven Fabric-Supported Photocatalysts. *Catalysts* **2020**, *10*, 304. [CrossRef]
11. Takanabe, K. Photocatalytic Water Splitting: Quantitative Approaches toward Photocatalyst by Design. *ACS Catal.* **2017**, *7*, 8006–8022. [CrossRef]
12. Takanabe, K.; Domen, K. Toward Visible Light Response: Overall Water Splitting Using Heterogeneous Photocatalysts. *Green* **2011**, *1*, 313–322. [CrossRef]
13. Khlyustova, A.; Sirotkin, N.; Kusova, T.; Kraev, A.; Titov, V.; Agafonov, A. Doped TiO_2: The Effect of Doping Elements on Photocatalytic Activity. *Mater. Adv.* **2020**, *1*, 1193–1201. [CrossRef]
14. Nur, A.S.M.; Sultana, M.; Mondal, A.; Islam, S.; Robel, F.N.; Islam, A.; Sumi, M.S.A. A Review on the Development of Elemental and Codoped TiO_2 Photocatalysts for Enhanced Dye Degradation under UV–Vis Irradiation. *J. Water Process Eng.* **2022**, *47*, 102728. [CrossRef]

15. Lu, C.-M.; Sharma, R.K.; Lin, P.-Y.; Huang, Y.-H.; Chen, J.-S.; Lee, W.-C.; Chen, C.-Y. Characteristics of Doped TiO2 Nanoparticle Photocatalysts Prepared by the Rotten Egg White. *Materials* **2022**, *15*, 4231. [CrossRef] [PubMed]
16. Asahi, R.; Morikawa, T.; Ohwaki, T.; Aoki, K.; Taga, Y. Visible-Light Photocatalysis in Nitrogen-Doped Titanium Oxides. *Science* **2001**, *293*, 269–271. [CrossRef] [PubMed]
17. Sirivallop, A.; Areerob, T.; Chiarakorn, S. Enhanced Visible Light Photocatalytic Activity of N and Ag Doped and Co-Doped TiO_2 Synthesized by Using an In-Situ Solvothermal Method for Gas Phase Ammonia Removal. *Catalysts* **2020**, *10*, 251. [CrossRef]
18. Yu, H.; Irie, H.; Hashimoto, K. Conduction Band Energy Level Control of Titanium Dioxide: Toward an Efficient Visible-Light-Sensitive Photocatalyst. *J. Am. Chem. Soc.* **2010**, *132*, 6898–6899. [CrossRef]
19. Huang, F.; Yan, A.; Zhao, H. Influences of Doping on Photocatalytic Properties of TiO2 Photocatalyst. In *Semiconductor Photocatalysis—Materials, Mechanisms and Applications*; IntechOpen: London, UK, 2016.
20. Karunakaran, C.; Abiramasundari, G.; Gomathisankar, P.; Manikandan, G.; Anandi, V. Cu-Doped TiO_2 Nanoparticles for Photocatalytic Disinfection of Bacteria under Visible Light. *J. Colloid Interface Sci.* **2010**, *352*, 68–74. [CrossRef]
21. Krishnakumar, V.; Boobas, S.; Jayaprakash, J.; Rajaboopathi, M.; Han, B.; Louhi-Kultanen, M. Effect of Cu Doping on TiO_2 Nanoparticles and Its Photocatalytic Activity under Visible Light. *J. Mater. Sci. Mater. Electron.* **2016**, *27*, 7438–7447. [CrossRef]
22. Alotaibi, A.M.; Williamson, B.A.D.; Sathasivam, S.; Kafizas, A.; Alqahtani, M.; Sotelo-Vazquez, C.; Buckeridge, J.; Wu, J.; Nair, S.P.; Scanlon, D.O.; et al. Enhanced Photocatalytic and Antibacterial Ability of Cu-Doped Anatase TiO_2 Thin Films: Theory and Experiment. *ACS Appl. Mater. Interfaces* **2020**, *12*, 15348–15361. [CrossRef] [PubMed]
23. Mathew, S.; Ganguly, P.; Rhatigan, S.; Kumaravel, V.; Byrne, C.; Hinder, S.J.; Bartlett, J.; Nolan, M.; Pillai, S.C. Cu-Doped TiO_2: Visible Light Assisted Photocatalytic Antimicrobial Activity. *Appl. Sci.* **2018**, *8*, 2067. [CrossRef]
24. Slamet, N.H.W.; Purnama, E.; Kosela, S.; Gunlazuardi, J. Photocatalytic Reduction of CO_2 on Copper-Doped Titania Catalysts Prepared by Improved-Impregnation Method. *Catal. Commun.* **2005**, *6*, 313–319. [CrossRef]
25. Colón, G.; Maicu, M.; Hidalgo, M.C.; Navío, J.A. Cu-Doped TiO_2 Systems with Improved Photocatalytic Activity. *Appl. Catal. B* **2006**, *67*, 41–51. [CrossRef]
26. Mingmongkol, Y.; Trinh, D.T.T.; Phuinthiang, P.; Channei, D.; Ratananikom, K.; Nakaruk, A.; Khanitchaidecha, W. Enhanced Photocatalytic and Photokilling Activities of Cu-Doped TiO_2 Nanoparticles. *Nanomaterials* **2022**, *12*, 1198. [CrossRef] [PubMed]
27. Xia, X.H.; Gao, Y.; Wang, Z.; Jia, Z.J. Structure and Photocatalytic Properties of Copper-Doped Rutile TiO_2 Prepared by a Low-Temperature Process. *J. Phys. Chem. Solids* **2008**, *69*, 2888–2893. [CrossRef]
28. Li, G.; Dimitrijevic, N.M.; Chen, L.; Rajh, T.; Gray, K.A. Role of Surface/Interfacial Cu^{2+} Sites in the Photocatalytic Activity of Coupled CuO−TiO_2 Nanocomposites. *J. Phys. Chem. C* **2008**, *112*, 19040–19044. [CrossRef]
29. López, R.; Gómez, R.; Llanos, M.E. Photophysical and Photocatalytic Properties of Nanosized Copper-Doped Titania Sol–Gel Catalysts. *Catal. Today* **2009**, *148*, 103–108. [CrossRef]
30. Zhang, W.; Li, Y.; Zhu, S.; Wang, F. Copper Doping in Titanium Oxide Catalyst Film Prepared by Dc Reactive Magnetron Sputtering. *Catal. Today* **2004**, *93–95*, 589–594. [CrossRef]
31. Bhattacharyya, K.; Mane, G.P.; Rane, V.; Tripathi, A.K.; Tyagi, A.K. Selective CO_2 Photoreduction with Cu-Doped TiO_2 Photocatalyst: Delineating the Crucial Role of Cu-Oxidation State and Oxygen Vacancies. *J. Phys. Chem. C* **2021**, *125*, 1793–1810. [CrossRef]
32. Razali, M.H.; Ahmad-Fauzi, M.N.; Mohamed, A.R.; Sreekantan, S. Hydrothermal synthesis and characterisation of Cu doped TiO_2 nanotubes for photocatalytic degradation of methyl orange. *Adv. Mat. Res.* **2014**, *911*, 126–130. [CrossRef]
33. Wu, M.-C.; Wu, P.-Y.; Lin, T.-H.; Lin, T.-F. Photocatalytic Performance of Cu-Doped TiO_2 Nanofibers Treated by the Hydrothermal Synthesis and Air-Thermal Treatment. *Appl. Surf. Sci.* **2018**, *430*, 390–398. [CrossRef]
34. Feng, S.-H.; Li, G.-H. Hydrothermal and Solvothermal Syntheses. In *Modern Inorganic Synthetic Chemistry*; Elsevier: Amsterdam, The Netherlands, 2017; pp. 73–104.
35. Deki, S.; Aoi, Y.; Yanagimoto, H.; Ishii, K.; Akamatsu, K.; Mizuhata, M.; Kajinami, A. Preparation and Characterization of Au-Dispersed TiO_2 Thin Films by a Liquid-Phase Deposition Method. *J. Mater. Chem.* **1996**, *6*, 1879. [CrossRef]
36. Maki, H.; Okumura, Y.; Ikuta, H.; Mizuhata, M. Ionic Equilibria for Synthesis of TiO_2 Thin Films by the Liquid-Phase Deposition. *J. Phys. Chem. C* **2014**, *118*, 11964–11974. [CrossRef]
37. Herbig, B.; Löbmann, P. TiO_2 Photocatalysts Deposited on Fiber Substrates by Liquid Phase Deposition. *J. Photochem. Photobiol. A Chem.* **2004**, *163*, 359–365. [CrossRef]
38. Yu, H.; Lee, S.C.; Yu, J.; Ao, C.H. Photocatalytic Activity of Dispersed TiO_2 Particles Deposited on Glass Fibers. *J. Mol. Catal. A Chem.* **2006**, *246*, 206–211. [CrossRef]
39. Listiani, P.S.; Honda, M.; Oya, H.; Horio, Y.; Ichikawa, Y. Optimization of Hydrolysis Temperature in Liquid Phase Deposition for TiO_2 Photocatalysis. *Jpn. J. Appl. Phys.* **2022**, *61*, 075508. [CrossRef]
40. Li, H.; Liu, B.; Yin, S.; Sato, T.; Wang, Y. Visible Light-Driven Photocatalytic Activity of Oleic Acid-Coated TiO_2 Nanoparticles Synthesized from Absolute Ethanol Solution. *Nanoscale Res. Lett.* **2015**, *10*, 415. [CrossRef]
41. Challagulla, S.; Tarafder, K.; Ganesan, R.; Roy, S. Structure Sensitive Photocatalytic Reduction of Nitroarenes over TiO_2. *Sci. Rep.* **2017**, *7*, 8783. [CrossRef]
42. Patterson, A.L. The Scherrer Formula for X-Ray Particle Size Determination. *Phys. Rev.* **1939**, *56*, 978–982. [CrossRef]

43. Durante, O.; Di Giorgio, C.; Granata, V.; Neilson, J.; Fittipaldi, R.; Vecchione, A.; Carapella, G.; Chiadini, F.; DeSalvo, R.; Dinelli, F.; et al. Emergence and Evolution of Crystallization in TiO_2 Thin Films: A Structural and Morphological Study. *Nanomaterials* **2021**, *11*, 1409. [CrossRef] [PubMed]
44. Liu, M.; Yu, S.; He, L.; Ni, Y. Recent Progress on Crack Pattern Formation in Thin Films. *Soft Matter* **2022**, *18*, 5906–5927. [CrossRef] [PubMed]
45. Louwerse, M.J.; Piccinini, M.; De Jong, K.P. Diffusion Mechanisms for Ions over Hydroxylated Surfaces: Cu on γ-Al $_2$ O $_3$. *J. Phys. Chem. C* **2019**, *123*, 18502–18507. [CrossRef]
46. Liu, D.; Flewitt, P.E.J. Chapter 5. Raman Measurements of Stress in Films and Coatings. *Prop. Inorg. Organomet. Compd.* **2004**, *45*, 141–177.
47. Scanlon, D.O.; Dunnill, C.W.; Buckeridge, J.; Shevlin, S.A.; Logsdail, A.J.; Woodley, S.M.; Catlow, C.R.A.; Powell, M.J.; Palgrave, R.G.; Parkin, I.P.; et al. Band Alignment of Rutile and Anatase TiO_2. *Nat. Mater.* **2013**, *12*, 798–801. [CrossRef] [PubMed]
48. Brus, L. Electronic Wave Functions in Semiconductor Clusters: Experiment and Theory. *J. Phys. Chem.* **1986**, *90*, 2555–2560. [CrossRef]
49. Thompson, T.L.; Yates, J.T. TiO_2-Based Photocatalysis: Surface Defects, Oxygen and Charge Transfer. *Top. Catal.* **2005**, *35*, 197–210. [CrossRef]
50. Honda, M.; Saito, Y.; Kawata, S. Individual TiO_2 Nanocrystals Probed by Resonant Rayleigh Scattering Spectroscopy. *Appl. Phys. Express* **2014**, *7*, 112402. [CrossRef]
51. Reckers, P.; Dimamay, M.; Klett, J.; Trost, S.; Zilberberg, K.; Riedl, T.; Parkinson, B.A.; Brötz, J.; Jaegermann, W.; Mayer, T. Deep and Shallow TiO_2 Gap States on Cleaved Anatase Single Crystal (101) Surfaces, Nanocrystalline Anatase Films, and ALD Titania Ante and Post Annealing. *J. Phys. Chem. C* **2015**, *119*, 9890–9898. [CrossRef]
52. Zhu, L.; Lu, Q.; Lv, L.; Wang, Y.; Hu, Y.; Deng, Z.; Lou, Z.; Hou, Y.; Teng, F. Ligand-Free Rutile and Anatase TiO_2 Nanocrystals as Electron Extraction Layers for High Performance Inverted Polymer Solar Cells. *RSC Adv.* **2017**, *7*, 20084–20092. [CrossRef]
53. Jackman, M.J.; Thomas, A.G.; Muryn, C. Photoelectron Spectroscopy Study of Stoichiometric and Reduced Anatase TiO_2 (101) Surfaces: The Effect of Subsurface Defects on Water Adsorption at Near-Ambient Pressures. *J. Phys. Chem. C* **2015**, *119*, 13682–13690. [CrossRef]
54. You, M.; Kim, T.G.; Sung, Y.-M. Synthesis of Cu-Doped TiO_2 Nanorods with Various Aspect Ratios and Dopant Concentrations. *Cryst. Growth Des.* **2010**, *10*, 983–987. [CrossRef]
55. Liu, M.; Qiu, X.; Miyauchi, M.; Hashimoto, K. Cu(II) Oxide Amorphous Nanoclusters Grafted Ti^{3+} Self-Doped TiO_2: An Efficient Visible Light Photocatalyst. *Chem. Mater.* **2011**, *23*, 5282–5286. [CrossRef]
56. Hu, Q.; Huang, J.; Li, G.; Chen, J.; Zhang, Z.; Deng, Z.; Jiang, Y.; Guo, W.; Cao, Y. Effective Water Splitting Using CuO_x/TiO_2 Composite Films: Role of Cu Species and Content in Hydrogen Generation. *Appl. Surf. Sci.* **2016**, *369*, 201–206. [CrossRef]
57. Francisco, M.S.P.; Mastelaro, V.R.; Nascente, P.A.P.; Florentino, A.O. Activity and Characterization by XPS, HR-TEM, Raman Spectroscopy, and BET Surface Area of CuO/CeO_2-TiO_2 Catalysts. *J. Phys. Chem. B* **2001**, *105*, 10515–10522. [CrossRef]

Disclaimer/Publisher's Note: The statements, opinions and data contained in all publications are solely those of the individual author(s) and contributor(s) and not of MDPI and/or the editor(s). MDPI and/or the editor(s) disclaim responsibility for any injury to people or property resulting from any ideas, methods, instructions or products referred to in the content.